Electronic Supplementary Material (ESI) for ChemComm.

Supporting Information for

Grain-Boundary-Rich Layered Double Hydroxide *via* a Boron-Assisted Strategy for Oxygen Evolution Reaction

Xiaohan Hou,† Huibin Liu,† Qicheng Zhang, Tiantian Fang, Minghong Sun, Wenchao Peng, Yang Li, Fengbao Zhang and Xiaobin Fan*

School of Chemical Engineering and Technology, State Key Laboratory of Chemical Engineering, Collaborative Innovation Center of Chemical Science and Engineering, Tianjin University, Tianjin 300072, People's Republic of China.

Experimental section

Materials preparation

Nickel nitrate ($Ni(NO_3)_2{\cdot}6H_2O$), ferric nitrate ($Fe(NO_3)_3{\cdot}9H_2O$), Polyvinylpyrrolidone (PVP, MW=30 K), sodium borohydride ($NaBH_4$), 60% sodium hydride (NaH) in oil, potassium hydroxide (KOH), Nafion solution (5 wt%) and Ketjen Black (KB) were purchased from Aladdin Ltd (Shanghai, China).
All reagents were of analytical grade and used directly.

Synthesis of g-NiFe-LDH-t (t=0 h, 0.2 h, 6 h and 24 h)

The g-NiFe-LDH-t nanosheets were prepared by the boron-assisted strategy. The amorphous borides/borates were produced in nitrogen environment following by a complete oxidation process into NiFe LDHs. In a typical synthesis, $Ni(NO_3)_2{\cdot}6H_2O$ (0.16 mmol), $Fe(NO_3)_3{\cdot}9H_2O$ (0.08 mmol) and PVP (700 mg) dissolved in deionized water (200 ml) in a beaker. The solution was deaerated with argon at room temperature. Then, the solution was injected into a 1000 mL round-bottom flask with 0.034 g $NaBH_4$ in static vacuum under continuous stirring. Pay attention to isolating oxygen to avoid potential dangers. After 10 min reaction under static vacuum, the resulting black solution was exposed to air for different time (0 h,0.2 h, 6 h and 24 h). The product was collected by filtration and washed by ethanol and water several times. The product was then dried at 60 ℃ in a vacuum oven for 6 h. The resultant products were denoted as g-NiFe-LDH-t (t=0 h, 0.2 h, 6 h and 24 h).

Equivalent $Co(NO_3)_2{\cdot}6H_2O$ was instead of $Ni(NO_3)_2{\cdot}6H_2O$ to prepare g-CoFe-LDH-24 h. Similarly, g-CoAl-LDH-24 h and g-CoFe-LDH-24 h were synthesized using other nitrates instead of $Ni(NO_3)_2{\cdot}6H_2O$ and $Fe(NO_3)_3{\cdot}9H_2O$.

Synthesis of NiFe-LDH-H, NiFe-LDH-B and NiFe-LDH-10B

NiFe-LDH-H, NiFe-LDH-B and NiFe-LDH-10B were synthesized by a similar protocol to g-NiFe-LDH-t except that the 0.034 g $NaBH_4$ was superseded by equivalent NaH (NiFe-LDH-H), equivalent NaH and equivalent borax (NiFe-LDH-B), equivalent NaH and 10 equivalent borax (NiFe-LDH-10B). NaH must avoid to contact with water in oxygen environment as it spontaneous combust violently. The product was collected by filtration and washed by ethanol and water several times. The product was then dried at 60 ℃ in a vacuum oven for 6 h.

Synthesis of traditional hydrothermal NiFe LDHs

The traditional hydrothermal NiFe LDHs were synthesized using a typical hydrothermal method.[S1] $Fe(NO_3)_3{\cdot}9H_2O$ (1.5 mmol), $Ni(NO_3)_2{\cdot}6H_2O$ (3.0 mmol),10 mmol of NH_4F and 12.5 mmol of urea were dissolved in 70 mL deionized water by ultrasound for 30 min. The resultant solution was transferred into a 100 mL of Teflon-lined stainless-steel autoclave. The autoclave was pre-heated to 120 °C, kept for 6 h and naturally cooled down. The product was collected by filtration and washed by ethanol and water several times. The product was then dried at 60 ℃ in a vacuum oven for 6 h.

Catalyst characterization

X-ray diffraction (XRD, D-8 Focus, Bruker Axs) was used to analyze the crystalline phases at a scanning rate of 8.5 s^{-1} using Cu-Ka radiation. Raman spectroscopy (LabRAM HR Evolution with 532 nm laser excitation, Horiba) further confirmed the sample type. The morphologies were examined by scanning electron microscopy (SEM, S-4800, HITACHI). The microstructures of the products were characterized by transmission electron microscopy (TEM, JEM-2100F, JEOL). The surface compositions and valence states of the samples were analyzed with X-ray photoelectron spectroscopy (Thermo Scientific K-Alpha).

Electrochemical Measurements

The electrochemical performance of the catalysts was evaluated in 1.0 M KOH using a three-electrode electrochemical cell on CHI 760E electrochemical analyzer (Chenhua, Shanghai). In a typical preparation of the working electrode, a powder with 3.5 mg catalyst and 1.5 mg KB was dispersed in a 1 mL solution with Nafion solution (35 μL, 5 wt.%), water (600 μL) and ethanol (365 μL). A homogeneous ink formed after 30 min ultrasonication. 5 μL of the ink was drop-cast onto the surface of a glassy-carbon electrode (GCE) which had a diameter of 3 mm to yield a catalyst loading of 0.248 mg cm^{-2}. The working electrode was air-dried for 30 min under ambient conditions. The electrochemical impedance spectroscopy (EIS) tests were carried out with the frequency ranging from 0.1 to 100 kHz at 1.485 V (vs. RHE). Rs was estimated from the resulting Nyquist plot and used for ohmic drop correction based on the relation $E_c = E_{(Ag/AgCl)} - iR_s$, where E_c is iR-corrected potential and i is the current corresponds to the $E_{(Ag/AgCl)}$. The saturated Ag/AgCl and graphite rod were used, respectively, as the reference electrode and counter electrode. The reversible hydrogen electrode (RHE) was calculated by the following formula: $E_{RHE} = E_c + 0.059 \times pH + 0.197\ V$. According to RHE, the overpotential (η) was calculated by $\eta = E_{RHE} - 1.23\ V$. Linear sweep voltammetry (LSV) was tested at a rate of 5 mV s^{-1} with potential range from 1.1 V to 1.8 V (vs. RHE). According to LSV, the Tafel plots were figured out by the formula: $\eta = a + b \lg j$, where η is overpotential, j is the current density, and b is the Tafel slope. Amperometric i-t curve was tested under 270 mV for 20 mA cm^{-2} and 650 mV for 300 mA cm^{-2}. Cyclic voltammetry (CV) curves were collected in non-faradic region with scan rates of 20 mV s^{-1} to 120 mV s^{-1} from 1.11 V to 1.21 V (vs. RHE).[S2, S3] In order to explore whether intrinsic activity is increased, the OER curves were normalized by ECAS with the formula: $ECSA\text{–} normalized\ current\ density = current\ density \times C_s/C_{dl}$, where C_s is the specific capacitance. In this work, C_s is 0.3 mF cm^{-2} for LDHs.[S4]

Computational details

All DFT calculations were conducted with Vienna ab-initio simulation package (VASP).[S5] Projector augmented wave (PAW) method was used to estimate the interactions between inner core and valence electrons.[S6] Perdew-Burke-Ernzerhof functional was adopted to calculated the exchange and correlation energies.[S7] Cutoff Energy and k-point were set to 520 eV and 1×1×1 Monkhorst-Pack grid. The Convergence criteria of energy and force during the optimization were 1.0×10^{-5} eV and 0.02 eV/Å, respectively.

Actually, it is difficult to construct the true structure of the LDH with GBs because of the uncertainty and irregularity of the atoms around the GBs. Here we fixed some metal atoms to describe the character of GBs, which is common in DFT calculations. The H atoms was removed to simplify the computational process.[S8]

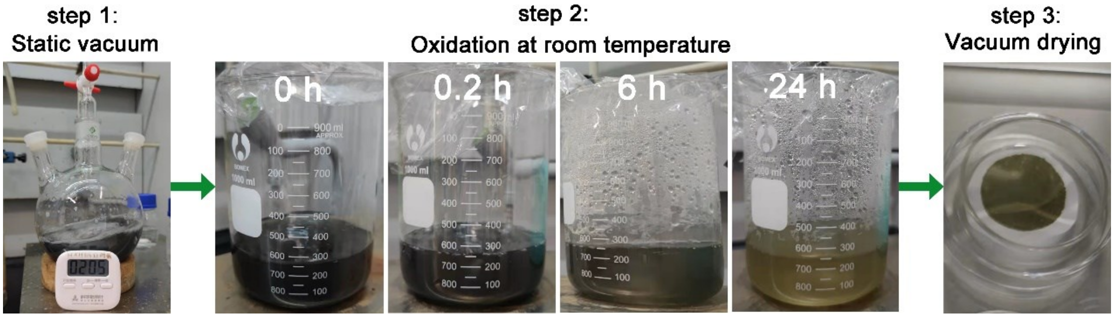

Fig. S1 Optical images of the boron-assisted strategy for grain-boundary-rich NiFe LDHs.

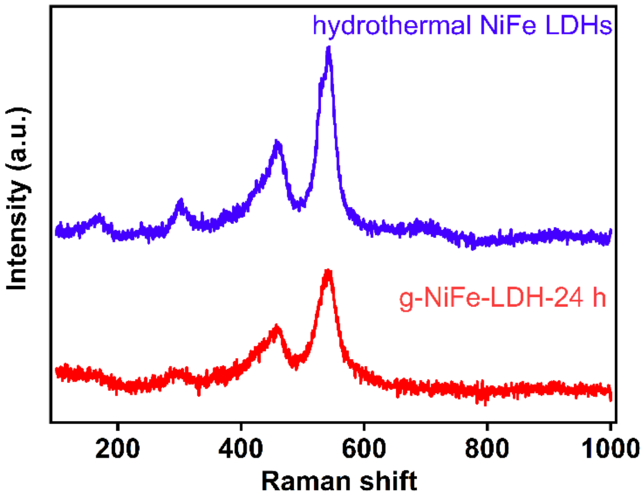

Fig. S2 Raman spectra of g-NiFe-LDH-24 h and traditional hydrothermal NiFe LDHs.

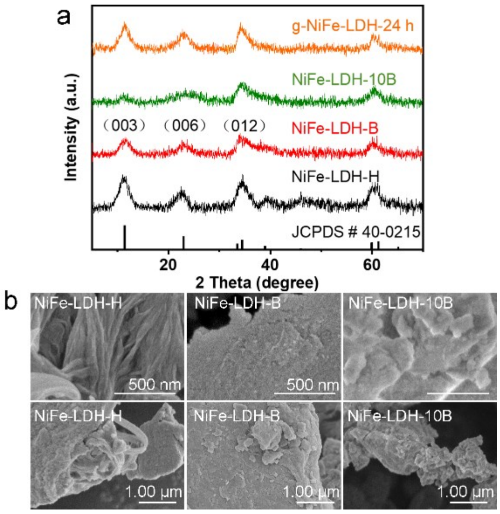

Fig. S3 (a) XRD patterns of g-NiFe-LDH-24 h, NiFe-LDH-H, NiFe-LDH-B and NiFe-LDH-10B. (b) SEM images of g-NiFe-LDH-24 h, NiFe-LDH-H, NiFe-LDH-B and NiFe-LDH-10B.

The effect of borohydride ($NaBH_4$) was investigated by XRD and SEM. Under the same condition, sodium hydride (NaH) instead of sodium $NaBH_4$ was used for synthesizing other control samples including NiFe-LDH-H (with no borax), NiFe-LDH-B (with equivalent borax) and NiFe-LDH-10B (with

10 equivalent borax). The XRD patterns of these samples (Fig. S3a) are similar and are all assigned to NiFe LDHs (JCPDS #40-0215), while the peak intensity of (003) decreases gradually with the increase of borax, indicating that the presence of borate can affect the orientation of LDHs. Whereas the XRD patterns confirm they are all LDHs phases, SEM images (Fig. S3b) show severely compacted, agglomerated morphologies completely different from that of g-NiFe-LDH. Therefore, in the formation of ultrathin g-NiFe-LDH-24 h, $NaBH_4$ plays an irreplaceable role in including but not limited to reduction and orientation.

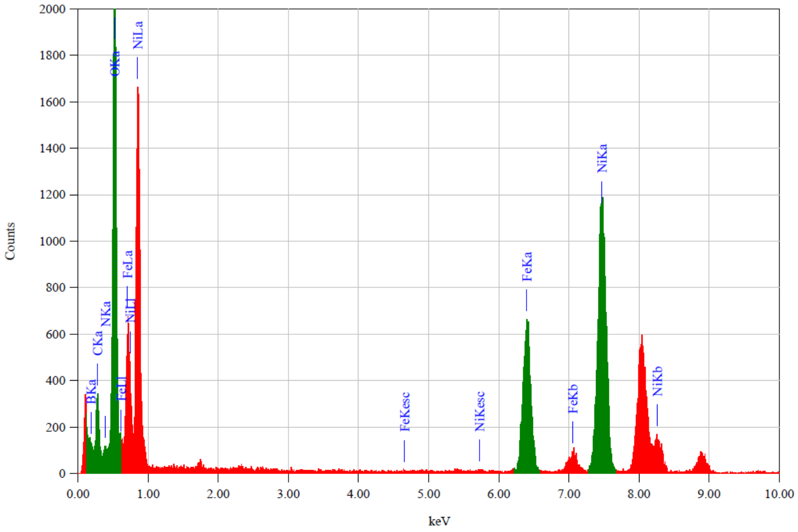

Fig. S4 Energy dispersive X-ray (EDX) spectrum of g-NiFe-LDH-24 h.

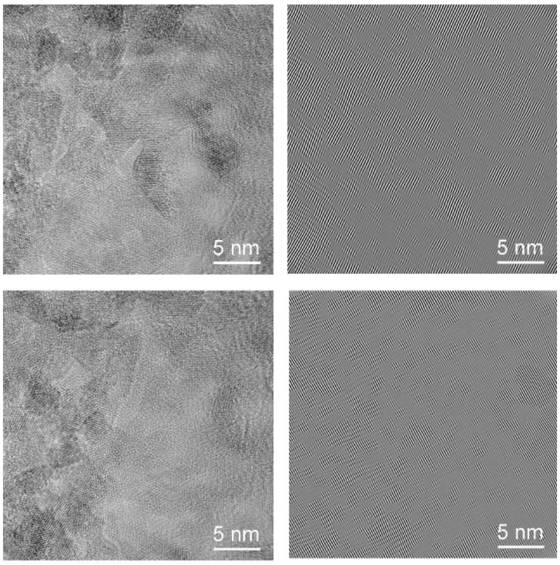

Fig. S5 TEM images of g-NiFe-LDH-24 h (left) and after IFFT (right) suggest that there are numerous GBs.

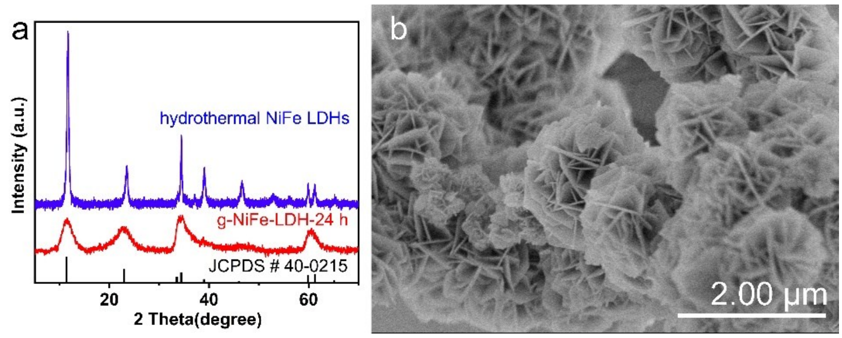

Fig. S6 (a) XRD patterns of traditional hydrothermal NiFe LDHs and g-NiFe-LDH-24 h. (b) SEM image of traditional hydrothermal NiFe LDHs.

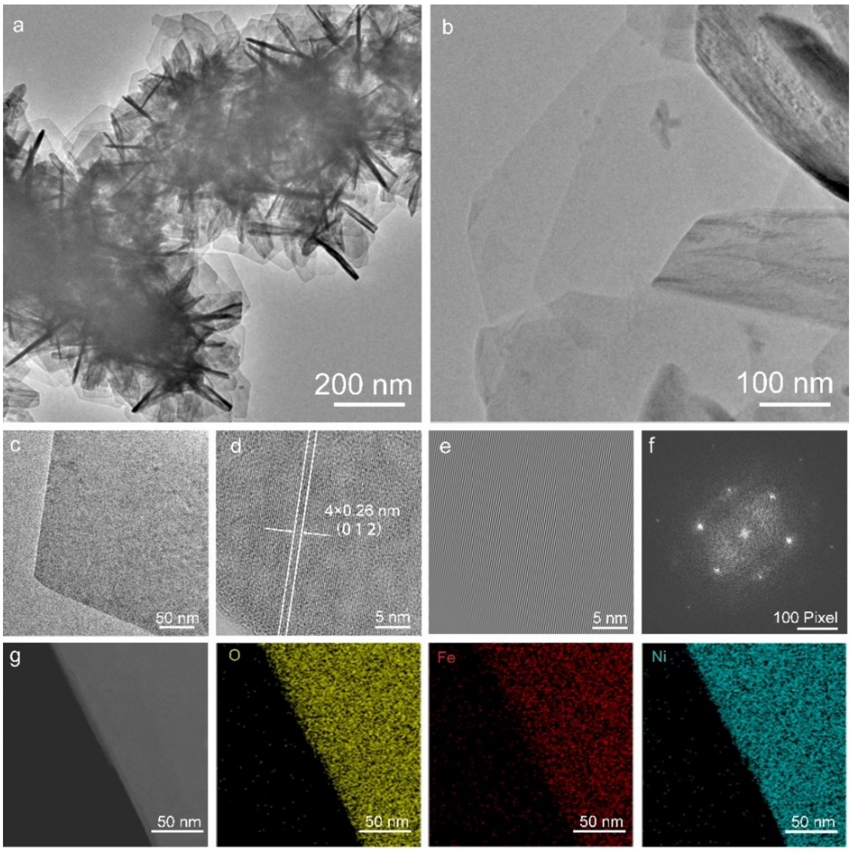

Fig. S7 (a-c) TEM, (d) HRTEM, (e) IFFT, (f) FFT and (g) dark-field TEM images and corresponding EDX mapping image for Fe (red), Ni (cyan) and O (yellow) for traditional hydrothermal NiFe LDHs. Fig. S7d and S7e show the perfect lattice without any GBs.

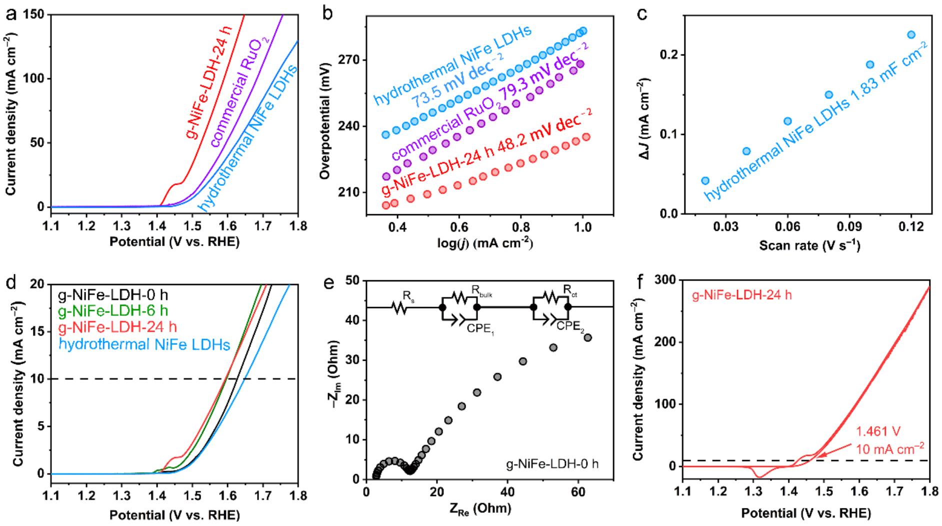

Fig. S8 (a) LSV curves and (b) Tafel slopes of g-NiFe-LDH-24 h, commercial RuO_2 and traditional hydrothermal NiFe LDHs. (c) C_{dl} values of traditional hydrothermal NiFe LDHs using CV measured. (d) ECSA-normalized LSV curve for g-NiFe-0 h, 6 h, 24 h and traditional hydrothermal NiFe LDHs. (e) Nyquist plot of g-NiFe-LDH-0 h and its equivalent circuit model show there is no GBs in g-NiFe-LDH-0 h. (f) CV curve from 1.1 to 1.8 V to obtain η_{10} of g-NiFe-LDH-24 h.

Fig. S8a, b show the η_{20} and Tafel slope of g-NiFe-LDH-24 h is much lower than those of commercial RuO_2 and traditional hydrothermal NiFe LDHs. ECSA-normalized LSV was used to investigate the intrinsic activity in catalysts. As shown in Fig. S8d, the intrinsic activity of g-NiFe-LDH-24 h has significantly increase compared with g-NiFe-LDH-0 h and traditional hydrothermal NiFe LDHs, which may be due to the formation of GBs. The electron distribution around GBs can be tuned efficiently due to the peculiar coordination number, and the intrinsic catalytic activity of active sites should be improved.

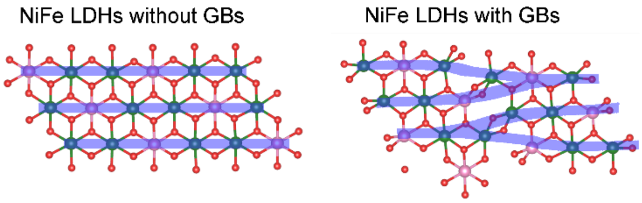

Fig. S9 Structure models of NiFe LDHs without (left) and with (right) GBs. "Y" shape spiral dislocations can be observed visually in NiFe LDHs with GBs.

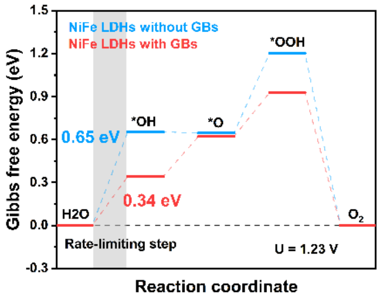

Fig. S10 Gibbs free energy diagram for the four steps of OER on NiFe LDHs without GBs site and with GBs site.

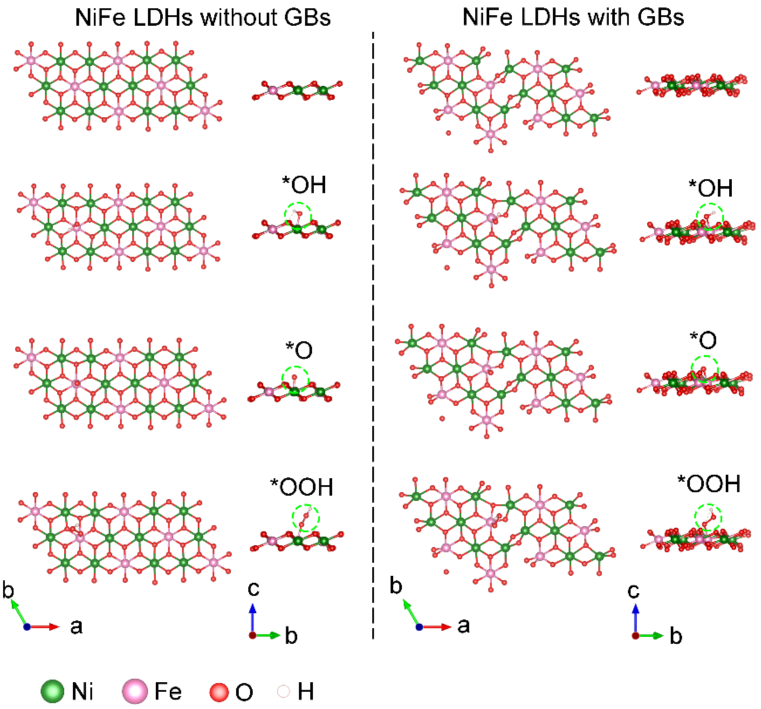

Fig. S11 Proposed 4e$^-$ mechanism of OER on NiFe LDHs without and with GBs. The Fe ion in the (003) crystal plane is the active site.[S2]

In order to further understand the OER activity enhancement of g-NiFe-LDH-24 h, DFT calculations were carried out to investigate the effects of GBs. The structure model of NiFe LDHs without and with GBs is exhibited in Fig. S9 and the “Y” shape spiral dislocations can be easily observed in NiFe LDHs with GBs (right). The Gibbs free energy diagram of the four steps OER process is shown in Fig. S10 and the corresponding adsorption models are displayed in Fig. S11. For the two samples, the rate-determining step is the first electron transfer step, which is common in LDHs. Although the key step is same, the NiFe LDHs with GBs hold a much smaller energy barrier (0.34 eV) than that without GBs (0.65 eV). According to the adsorption energy of the three intermediates (*OH, *O, *OOH), NiFe LDHs with GBs provide stronger binding strength, thus, the *OH formation steps (rate-determining step) are readily accessible. Therefore, we speculate that the strong adsorption which origins from the unsaturated metal atom around the GBs can increase OER activity.

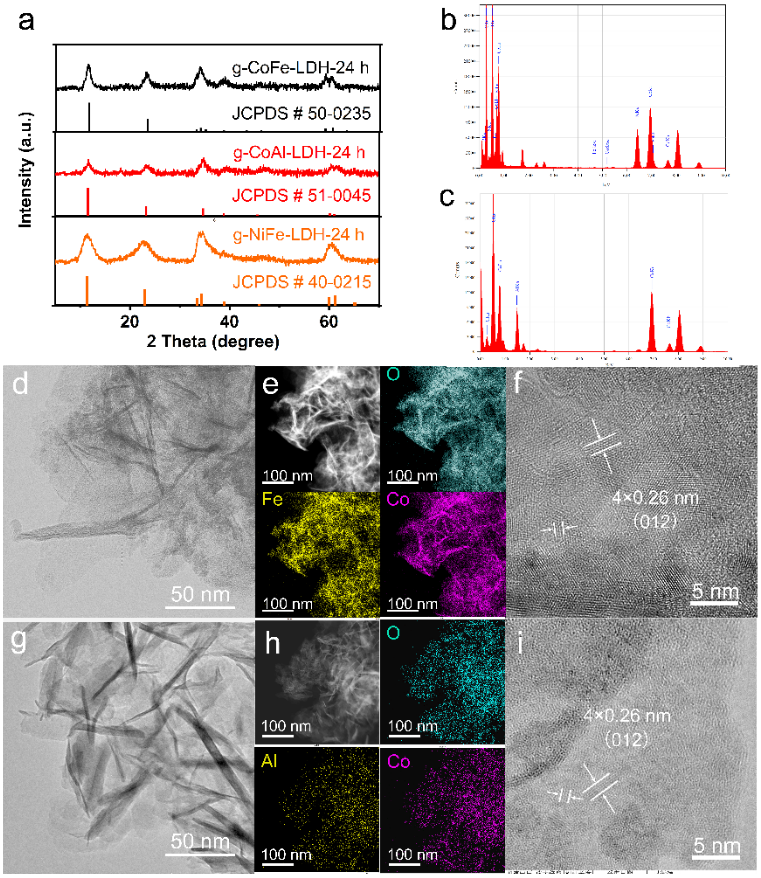

Fig. S12 (a) XRD patterns of g-CoFe-LDH-24 h, g-CoAl-LDH-24 h and g-NiFe-LDH-24 h via the boron-assisted strategy. (b) Energy dispersive X-ray (EDX) spectrum, (d) TEM images, (e) Dark-field TEM image and corresponding EDX mapping image, O (cyan), Fe (yellow) and Co (pink)), (f) HRTEM images for g-CoFe-LDH-24 h. (c) Energy dispersive X-ray (EDX) spectrum, (g) TEM images, (h) Dark-field TEM image and corresponding EDX mapping image, O (cyan), Al (yellow) and Co (pink)), (i) HRTEM images for g-CoAl-LDH-24 h.

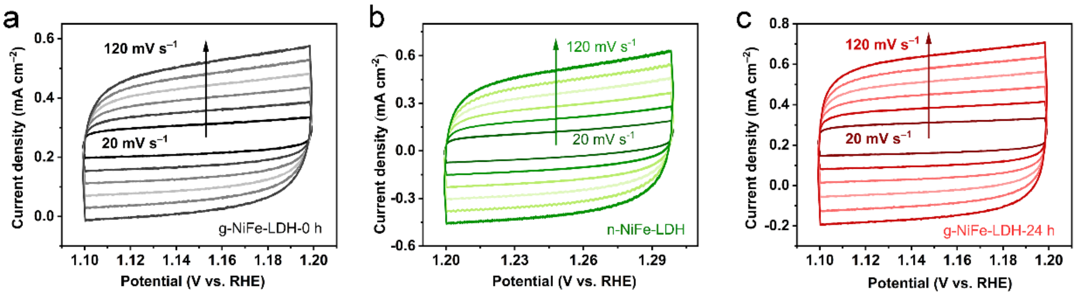

Fig. S13. The cyclic voltammograms of (a) g-NiFe-LDH-0 h, (b) g-NiFe-LDH-6 h and (c) g-NiFe-LDH-24 h.

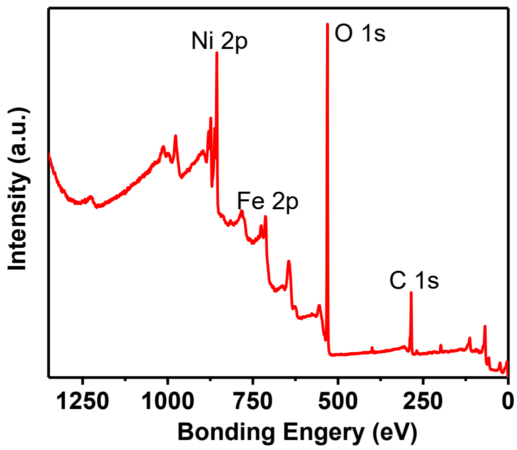

Fig. S14 XPS spectra of g-NiFe-LDH-24 h.

Table S1. The atomic ratio for g-NiFe-LDH-24 h obtained by EDX.

Element	(KeV)	Mass%	Counts	Sigma	Atom%
B K		N.D.			N.D.
C K	0.227	6.88	1224.33	0.15	15.28
N K	0.392	0.37	112.78	0.05	0.71
O K	0.525	34.15	14408.95	0.36	56.95
Fe K	6.398	18.14	8694.50	0.32	8.67
Ni K (Ref.)	7.471	40.46	17228.18	0.51	18.39
Total		100.00			100.00

Table S2. Comparison of OER activity between g-NiFe-LDH and reported electrocatalysts.

Catalyst	Electrolyte	Electrode	Current density (mA cm^{-2})	Overpotential (mV)	Reference
NiFeMn LDHs	1 M KOH	CFP	20	289	S9
NiFe-LDH hollow microspheres	1 M KOH	GCE	10	239	S10
NiFe LDH nanosheets	1 M KOH	Cu foil	10	260	S11
NiFe LDH with Ni-defects	1 M KOH	GCE	10	239	S12
Ni/Ni(OH)$_2$ heterostructured nanosheets	1 M KOH	nickel foam	10	270	S13
Ni–Fe–Ce-LDH microcapsules	1 M KOH	GCE	10	242	S14
Precovered NiFe LDH	1 M KOH	GCE	10	243	S15
FeNi$_3$–B/G nanosheet	1 M KOH	GCE	10	230	S16
NixB nanosheets	1 M KOH	GCE	10	380	S17
Commercial RuO$_2$	1 M KOH	GCE	20	300	This work
g-NiFe-LDH-24 h	1 M KOH	GCE	20	244	This work
	1 M KOH	GCE	10	231	This work

Glass carbon electrode (GCE). Carbon fiber paper (CFP). All based on geometric normalized.

Table S3. R_s, R_{bulk}, R_g and R_{ct} calculated by fitting of the impedance data with the equivalent circuit model.

	R_s/Ω	R_{bluk}/Ω	R_g/Ω	R_{ct}/Ω
g-NiFe-LDH-0 h	2.66	9.10	0.00	130.00
g-NiFe-LDH-6 h	2.88	6.14	24.50	12.10
g-NiFe-LDH-24 h	2.51	6.29	14.50	4.19

Table S4. The atomic ratio obtained by XPS.

Sample	Name	Start BE/eV	Peak BE/eV	End BE/eV	Height/CPS	FWHM/eV	Atomic/%
g-NiFe-LDH-0 h	B 1s	195.98	191.52	180.18	669.59	1.12	3.26
	C 1s	297.98	284.71	279.18	23672.82	1.77	28.65
	Fe 2p	739.98	711.79	700.18	16553.01	6.39	8.71
	Ni 2p	887.98	855.61	844.18	48266.22	2.44	13.13
	O 1s	544.98	531.1	525.18	108852.97	1.82	46.24
g-NiFe-LDH-24 h	B 1s	195.98	184.77	180.18	509.77	0.36	2.75
	C 1s	297.98	284.82	279.18	26666.61	1.79	24.97
	Ni 2p	887.98	855.68	844.18	78267.26	2.40	16.01
	Fe 2p	739.78	712.18	700.08	20851.95	6.21	8.15
	O 1s	544.98	531.13	525.18	159566.84	1.73	48.11

REFERENCES

S1 X. Meng, J. Han, L. Lu, G. Qiu, Z. L. Wang and C. Sun, Small, 2019, 15, e1902551.

S2 Y.-N. Zhou, F.-L. Wang, S.-Y. Dou, Z.-N. Shi, B. Dong, W.-L. Yu, H.-Y. Zhao, F.-G. Wang, J.-F. Yu and Y.-M. Chai, Chemical Engineering Journal, 2022, 427.

S3 Y.-N. Zhou, W.-L. Yu, Y.-N. Cao, J. Zhao, B. Dong, Y. Ma, F.-L. Wang, R.-Y. Fan, Y.-L. Zhou and Y.-M. Chai, Applied Catalysis B: Environmental, 2021, 292.

S4 F. Dionigi, J. Zhu, Z. Zeng, T. Merzdorf, H. Sarodnik, M. Gliech, L. Pan, W. X. Li, J. Greeley and P. Strasser, Angew Chem Int Ed Engl, 2021, 60, 14446-14457.

S5 G. Kresse and J. Furthmuller, Phys Rev B Condens Matter, 1996, 54, 11169-11186.

S6 P. E. Blochl, Phys Rev B Condens Matter, 1994, 50, 17953-17979.

S7 J. P. Perdew, K. Burke and M. Ernzerhof, Phys Rev Lett, 1996, 77, 3865-3868.

S8 X. Wang, Y. Tuo, Y. Zhou, D. Wang, S. Wang and J. Zhang, Chemical Engineering Journal, 2021, 403.

S9 Z. Lu, L. Qian, Y. Tian, Y. Li, X. Sun and X. Duan, Chem Commun (Camb), 2016, 52, 908-911.

S10 C. Zhang, M. Shao, L. Zhou, Z. Li, K. Xiao and M. Wei, ACS Appl Mater Interfaces, 2016, 8, 33697-33703.

S11 H. Yang, S. Luo, Y. Bao, Y. Luo, J. Jin and J. Ma, Inorganic Chemistry Frontiers, 2017, 4, 1173-1181.

S12 Y. Wang, M. Qiao, Y. Li and S. Wang, Small, 2018, 14, e1800136.

S13 L. Dai, Z. N. Chen, L. Li, P. Yin, Z. Liu and H. Zhang, Adv Mater, 2020, 32, e1906915.

S14 H. J. Xu, C. F. Shan, X. X. Wu, M. Z. Sun, B. L. Huang, Y. Tang and C. H. Yan, Energy & Environmental Science, 2020, 13, 2949-2956.

S15 C. C. Wu, H. Q. Li, Z. X. Xia, X. M. Zhang, R. Y. Deng, S. L. Wang and G. Q. Sun, Acs Catalysis, 2020, 10, 11127-11135.

S16 J. M. V. Nsanzimana, R. Dangol, V. Reddu, S. Duo, Y. Peng, K. N. Dinh, Z. Huang, Q. Yan and X. Wang, ACS Appl Mater Interfaces, 2019, 11, 846-855.

S17 J. Masa, I. Sinev, H. Mistry, E. Ventosa, M. de la Mata, J. Arbiol, M. Muhler, B. Roldan Cuenya and W. Schuhmann, Advanced Energy Materials, 2017, 7.